High-temperature electron microscopy study of ThO_2 microspheres sintering

G.I. Nkou Bouala, Nicolas Clavier, J. Léchelle, J. Monnier, Ch. Ricolleau, N. Dacheux, Renaud Podor

High-Temperature Electron Microscopy Study of ThO_2 Microspheres Sintering

G.I. Nkou Bouala [1], N. Clavier [1,*], J. Léchelle [2,3], J. Monnier [1], Ch. Ricolleau [4], N. Dacheux [1], R. Podor [1]

1- *ICSM, UMR 5257 CEA/CNRS/ENSCM/Université de Montpellier, Site de Marcoule - Bât. 426, BP 17171, 30207 Bagnols/Cèze cedex, France*

2- *CEA,DEN,DEC, Centre de Cadarache, 13108 St-Paul lez Durance, France*

3- *CEA,DEN,DTEC, Centre de Marcoule, 30207 Bagnols/Cèze, France*

4- *Laboratoire de Matériaux et Phénomènes Quantiques, Bâtiment Condorcet, CNRS UMR 7162, Université Paris Diderot, 75013 Paris, France*

*** Corresponding author :**
Dr. Nicolas CLAVIER
ICSM – UMR 5257 CEA/CNRS/UM/ENSCM
Site de Marcoule – Bât 426
BP 17171
30207 Bagnols sur Cèze
France

Phone : + 33 4 66 33 92 08
Fax : + 33 4 66 79 76 11

nicolas.clavier@icsm.fr

Abstract

The behavior of ThO_2 microspheres was investigated *in situ* at high temperature by electron microscopy, including HR-TEM and ESEM. The observation of isolated particles first allowed to describe the mechanisms driving the growth of crystallites within the microspheres, i.e. a combination of oriented attachment and solid-state diffusion, and to evaluate the associated activation energies.

Polycrystalline and single-crystal two-grain systems were further investigated to monitor the formation of a neck during heat treatment. For single crystals, the topological evolution was found to agree well with the models, whereas the establishment of neck between two polycrystalline microspheres deviated from the expected trend, with the formation of intermediate large-size crystallites. Such modification was mainly assigned to the microstructures of the particles used, showing that the level of polycrystallinity of the powder and its initial microstructure, which both arose from the synthesis method, must be considered carefully to evaluate its sintering capability.

Keywords

Sintering – *In situ* ESEM –Thorium oxide – Polycrystalline – Single crystal

1. Introduction

Thoria-based oxides present a great interest for their potential uses within the nuclear fuel cycle. First, ThO_2 could be envisaged as a fuel in an alternative to the UO_2 pellets currently used in Light Water Reactors (LWRs) [1]. Indeed, even if ^{232}Th is not a fissile isotope, it can be turned to the fertile ^{233}Th by neutron capture in the reactor. This latter further yields to fissile ^{233}U daughter product through two successive β^- disintegrations. Beyond the great natural abundance of thorium on earth [2,3], ThO_2 presents several physico-chemical properties of interest as a nuclear fuel, such as higher thermal conductivity and melting point compared to UO_2, which can both enhance the thermal yield and increase the tolerance to accidental situations [4]. On this basis, ThO_2-based fuel cycles have long been envisaged. Advanced projects are also developed within several countries, including India [5,6].

Besides, thoria was also envisaged as a matrix for the transmutation of minor actinides [7,8], as well as of the excess military weapon-grade plutonium coming from the dismantlement and disposition programs in Russia and USA [9]. Beyond its uses as a fuel, thoria was also investigated for its potentialities as a catalyst [10], electrode material [11] or fuel cell electrolyte. In this latter case, one can note that applications are also planned within future nuclear reactor concepts (such as those included in the Gen-IV program [12]), as thoria-based oxides are currently envisaged as electrolyte material within oxygen sensors to be operated in Sodium-cooled Fast Reactors (SFRs) [13,14].

In this framework, a renewed interest concerned the development of innovative routes for the synthesis of ThO_2-based materials. Such methods include the preparation of nanomaterials [15,16], morphology-controlled powders [17,18,19], and of low-temperature precursors that can yield the targeted material through high-temperature heat treatment [20,21]. However, if several efforts were made concerning synthesis, only few papers were recently devoted to the sintering of ThO_2 and related phases [22,23,24]. Moreover, they mainly concern the intermediate and final stages of the densification, which are characterized by the successive elimination of open then closed porosity.

On the other hand, the first stage of sintering, defined by the formation of necks between the grains that confers a mechanical coherence to the powder agglomerate, was mainly investigated through numerical simulations [25,26,27]. Among the various methods used, molecular dynamics [28], as well as Monte Carlo [29] and Discrete Elements methods [30] were frequently considered but involved some approximations on the grain morphology (supposed to be spherical) as well as on their crystalline state (single crystal). The results obtained can then hardly be used to provide a predictive and reliable description of the first stage of the sintering process that is needed if one wants to optimize the fabrication cycle of materials such as nuclear fuels. In this framework, an experimental method, based on the use of *in situ* observations performed thanks to High-Temperature Environmental Scanning Electron Microscopy (HT-ESEM) was developed and tested on model compounds [31].

This paper then reports a study of the sintering behavior of ThO_2 microspheres through HT-ESEM. The behavior of a single particle during heat treatment at high temperature was first investigated to monitor the evolution of the crystallite size within the microsphere and get a first insight about the associated mechanisms. The morphological modifications occurring

during the heat treatment of two microspheres in contact were then followed for both poly- and single-crystal particles. Processing the micrograph series allowed the quantification of several parameters of interest (grains and neck diameters, distance between the grains, etc.). Their variation versus temperature was then used to determine the mechanisms controlling the sintering of both systems and the corresponding activation energies.

2. Experimental

2.1. Synthesis and characterization of ThO_2 microspheres

The synthesis of thorium oxide powders with a spherical shape was performed through a hydrothermal route inspired from the protocol reported in the literature by Wang *et al.* [18]. During a typical synthesis, 2×10^{-4} mole of thorium nitrate pentahydrate (supplied by Sigma-Aldrich) was dissolved in 5 mL of deionized water. The as-obtained solution was then mixed with 10^{-4} mole of urea and 2.7×10^{-3} mole of glycerol, used as a complexing and shaping agents, respectively. After ageing for about 10 minutes under magnetic stirring, this mixture was transferred to a 12.5 mL Teflon-lined stainless steel autoclave (Parr), then heated in an oven at 120°C for various holding times ranging from 10 to 32 hours. A white precipitate was systematically obtained after heat treatment and separated from the supernatant by centrifugation at 4500 rpm, washed twice with deionized water and ethanol, and finely dried overnight in an oven at 60°C.

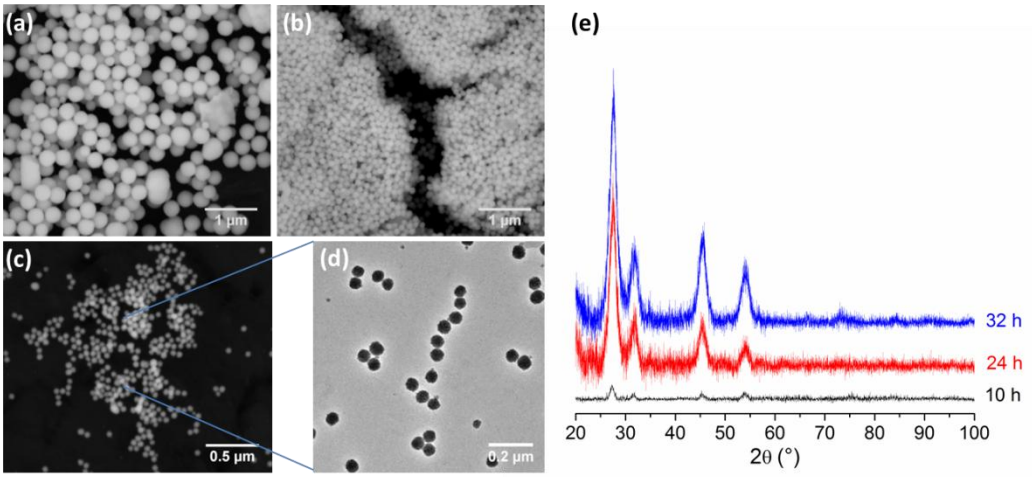

Figure 1 : SEM observations of ThO_2 microspheres obtained during hydrothermal synthesis at 120°C and for different heating times (a) 32 h; (b) 24 h; (c) 10 h; (d) TEM observation of ThO_2 nanospheres; (e) XRD patterns of ThO_2 samples.

The SEM and TEM observations performed on the samples (see details below) revealed that the precipitates were in any case made up of submicrometric microspheres, which diameter depends on the synthesis conditions **(Figure 1a-d)**, in good agreement with the results initially reported by Wang *et al.* [18]. Indeed, the size of $ThO_2.nH_2O$ microspheres increased with the hydrothermal heating time, the grains diameter being equal to about 50 nm after 10 hours at 120°C whereas it reached 400 nm for 32 hours of heating. Moreover, the microspheres appeared to be composed of smaller particles, probably corresponding to

elementary crystallites. Such hierarchical microstructure was already reported for other actinides-based samples exhibiting a spherical shape [18,32].

Powder X-Ray Diffraction (PXRD) patterns of the precipitates were obtained by the means of a Bruker D8 diffractometer equipped with a Lynx-eye detector adopting the parallel geometry (reflection mode), and using Cu $K\alpha_{1,2}$ radiation (λ = 1.54184 Å). PXRD patterns were recorded at room temperature in the $5° \leq 2\theta \leq 100°$ range, with a step size of $\Delta(2\theta) = 0.08°$ and a total counting time of about 1.5 hours. Whatever the hydrothermal treatment duration, the PXRD patterns recorded exhibited wide PXRD lines (large FWHM) corresponding to the cubic fluorite-type structure (Fm-3m space group), characteristic of actinide dioxides [33] **(Figure 1e)**. Such pattern was assigned to the precipitation of $ThO_2.nH_2O$ hydrated oxide based on obvious similarities with other actinide-based compounds in the literature, including $UO_2.2H_2O$ [34]. Also, the important width of the PXRD peaks can be ascribed to the partly amorphous and/or nanocrystalline character of the powder. This latter point agrees well with the preparation of polycrystalline samples exhibiting a hierarchical microstructure made of small crystallites assembled within microspheres.

The formulation of the samples was further precised thanks to thermogravimetric analyses performed with a Setaram Setsys Evolution apparatus (10°C.min^{-1}, air atmosphere). Indeed, a global weight loss of about 12% was observed after heating above 600°C, which corresponds to the departure of 2 water molecules per formula unit (**Figure S1**). Once again, the obtained nanocrystalline $ThO_2.2H_2O$ appeared in good agreement with the previous work reported concerning hydrated actinides dioxides [34,35].

Polycrystalline ThO_2 microspheres were then finally prepared by thermal conversion of the precursors at 750 °C during 4 h under air. The SEM characterization (not presented here) did not reveal any significant modification of the morphology which still exhibited a spherical shape. Also, additional nitrogen adsorption measurements were performed at 77K thanks to a Micromeritics ASAP 2020 apparatus in order to evaluate the specific surface area of the powders (BET method). Prior to the measurements, the samples were dried at 150°C overnight to ensure their complete outgassing. The pore size distribution of the ThO_2 microspheres was also determined from the desorption branches of nitrogen adsorption isotherm according to the BJH (Barret, Joyner and Halenda) method, based on the Kelvin equation, which links the pore size with critical condensation pressure, by assuming a straight cylindrical pore model [36]. From these analyses, the specific surface area of the ThO_2 microspheres was evaluated as 60 $m^2.g^{-1}$, and presented several classes of mesopores with a diameter of 3-8 nm and an average size of 3.5 nm (see distribution presented on **Figure S2**). Such mesoporisity probably arose from the elimination of water molecules during the dehydration step [37] and led to a poral volume of about 6% within the microspheres.

2.2. Sample preparation and experimental procedures

As already reported in our previous work [31], sample preparation was undertaken prior to ESEM observations in order to obtain different kinds of geometrical configurations with the microspheres, that can be further used for the study of the first stage of sintering. In this aim,

5 mg of as-prepared powder ($ThO_2.2H_2O$ precursor) was dispersed into 1 mL of acetone; a drop of this mixture was then deposited at the surface of a 2 mm^2 Pt-Au10 thin foil. This preparation allowed the spontaneous formation of different grains assemblages, either constituted by an isolated single grain or by two or more grains in contact.

In situ high temperature experiments were further performed with a FEI Quanta 200 field-emission ESEM (Environmental Scanning Electron Microscopy) equipped with a 1500 °C hot stage [38,39]. The precise measure of the sample temperature was achieved using a custom thermocouple integrated in the sample holder [40]. Based on the values usually reported in the literature for the sintering of ThO_2, which typically ranges from 1500 [21] to 1750°C [41], *in situ* HT-ESEM experiments were performed between 1100 and 1300°C under air atmosphere composition at an operating pressure of about 250 Pa. In this range of temperatures, the image resolution decreased with the increase of operating temperature, mainly due to the vibrations induced by the water circuit cooling and the increase of thermal electrons production [42,43]. Prior to reaching the desired temperature, an isothermal dwell of 30 min. at 850-900°C was considered to ensure the dehydration of $ThO_2.H_2O$ precursor into anhydrous ThO_2 microspheres.

Our first experimental observations revealed that the neck formation between two ThO_2 microspheres began at about 1100 °C with a very slow kinetics. For these reasons, the first stage of sintering was also investigated by using an *ex situ* ESEM procedure [44], in parallel with the *in situ* experiments. The samples (ThO_2 microspheres onto Pt-Au10) were then rapidly introduced into a conventional furnace pre-heated at the required temperature and maintained isothermally for a few minutes. Such heat treatments were repeated several times, which allowed us to record high resolution SEM images after each heating run [44] with both secondary and backscattered electron modes, this latter being unavailable during *in situ* experiments. By this means, it was possible to achieve a statistical study of the evolution of the microspheres during heat treatment, by following the evolution of several systems during the same experiment.

Additional observations were also performed by HR-TEM experiments thanks to the advanced technology of the JEOL JEM-ARM200F which allowed unprecedented atomic scale analysis. This device combined a spherical aberration corrector CEOS™ and a cold field emission gun (CFEG) which allowed information transfer below 75 pm at 200 kV. These experimental conditions led to directly image the atomic arrangement of the samples along various indexes zone axis. For *in situ* high temperature observations, we used the Protochips Atmosphere specimen holder which allows heating from room temperature to 1200°C. The main advantage of this holder is its very high mechanical stability allowing high resolution imaging at high temperature. Prior to the observations, microspheres were simply deposited on the sample holder in a solvent droplet after ultrasonic dispersion. To enhance the signal to noise ratio in the images and since the experiment did not need gas environment, we slightly modified the configuration of the Atmosphere holder by breaking the large E-chips and the inlet and outlet gas lines of the holder were connected to a primary pumping system. In such a way, the electron beam went through only one membrane of Si_xN_{1-x} and the sample.

2.3. Image processing

The images recorded during the ESEM observations were then processed for the direct determination of the experimental data, characteristic of the morphological modifications occurring during heat treatments. Different methods were used depending on the type of system studied (typically, an isolated microsphere or a two-grain system) and the experimental data to be determined. In every case, the final data provided came from the average of 12 to 15 analyzed systems, the associated standard deviation being used as error bar.

For isolated microspheres, the images were processed through Fiji software [45,46]. This method allowed the determination of the evolution of several parameters during heat treatment, including crystallite and grain sizes. In this aim, the crystallites were first counted manually at the surface of the grain then the grain radius was evaluated by automatic grain contour extraction **(Figure 2a)**. Both parameters led to the direct determination, by simple mathematical calculation, of the average size of the crystallites included in the microspheres [44].

For the systems constituted by a two-grain assemblage, detailed image processing was reported in our previous publication [31]. First, the Trainable Weka Segmentation plugin [47] available in the Fiji software [46] was used for the automatic extraction of grain contours. The images obtained after segmentation were then used with custom software ImageJu [48] for the determination of different parameters generally used in numerical models to describe the morphological modifications occurring during the first stage of sintering, such as neck size, grains radii and dihedral angles **(Figure 2b)**.

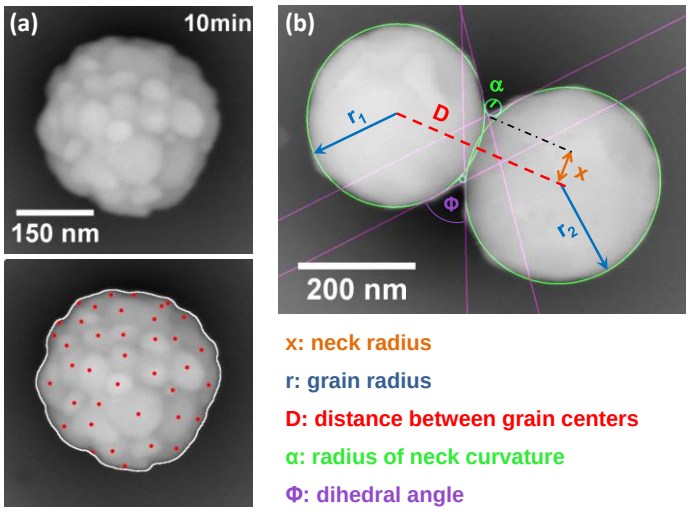

Figure 2 : SEM images processing : (a) determination of crystallites and grain size for a single grain system; (b) characteristic parameters retained to describe the first stage of sintering of a two-grain system.

3. Results and discussion

3.1. Microstructural evolution of isolated microspheres

The morphological modifications occurring during heat treatment of isolated polycrystalline microspheres were monitored during *ex situ* ESEM and *in situ* HT-HRTEM observations. They are clearly evidenced on the images series presented in **Figure 3** and are mainly due to the reorganization of the crystallites within the microspheres. Indeed, the number of crystallites within the microspheres gradually decreased during heat treatment until a single crystal (i.e. constituted by one crystallite) with spherical shape is obtained [49]. On this basis, and even if the number of crystallites initially present in the microspheres is modified throughout the heat treatment, the spherical morphology of the grains was found to be conserved [44] for the range 1200-1300°C **(Figure 3a)**, even if the shape of the particles evolves slightly towards a more cubic shape for the longer heating times considered.

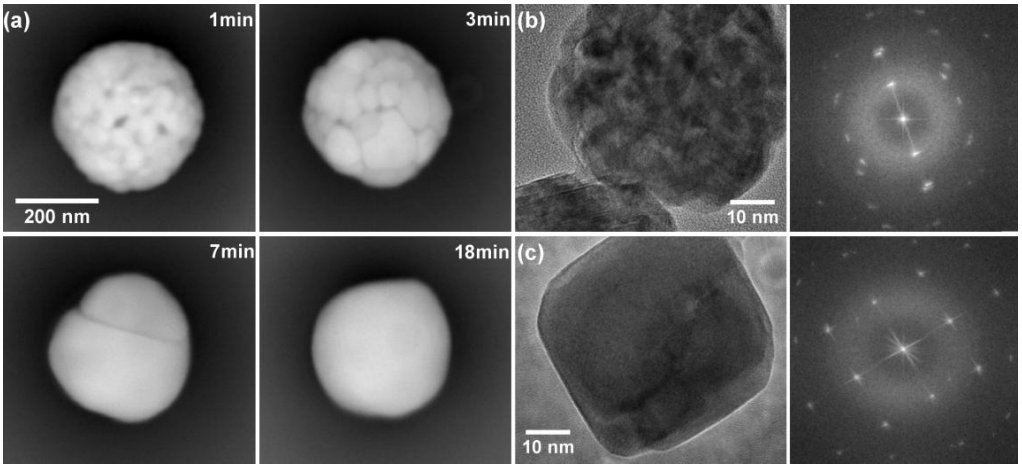

Figure 3 : (a) *Ex situ* ESEM image series of ThO_2 microsphere throughout heat treatment at T=1275°C; *in situ* TEM micrograph of (b) ThO_2 polycrystalline particle recorded after 25 min. at T=1000°C and (c) ThO_2 single crystal formed after 45 min. at T=1025°C with associated FFT images.

A similar behavior was observed by high resolution TEM (HRTEM), during the *in situ* isothermal treatment of ThO_2 microspheres of about 50 nm at 1100°C. As previously evidenced by ESEM, a gradual decrease of the crystallites number was observed during the heat treatment until a single crystal grain was obtained. Nevertheless, in the case of TEM observations, the electronic beam was found to significantly influence the kinetics of crystallite growth. Such bias precluded the determination of quantitative data but still allowed the use of the micrographs to describe qualitatively the morphological modifications occurring during the heat treatment. In this sense, the Fast Fourier Transformation (FFT) performed on the HRTEM micrographs clearly showed important variations in the orientation of atomic planes [50,51]. Indeed, at the beginning of the heat treatment, FFT consisted of rings (or arcs) characteristic of the presence of several crystallites with different orientations in the analyzed zone **(Figure 3b)**. All of them exhibited the typical pattern of a cubic structure, which fits well with the fluorite-type ThO_2. Conversely, the FFT pattern extracted

after 45 min. of heating at 1025°C image appeared typical of a single crystal **(Figure 3c)**. In this case, the determination of the various reflections allowed to show precisely the zone axis which demonstrated the orientation of the ThO_2 single crystal along the (100) plane.

Image processing was then further performed on SEM micrographs in order to quantify the morphological modification occurring in isolated microspheres during heating and led to plot the evolution of average crystallite size for different temperatures. As directly observed on the ESEM and HRTEM micrographs, the average crystallite size increases gradually during heat treatment **(Figure 4a)**, which was correlated to a decrease in the crystallites number **(Figure 4b).** Both kinetics were significantly influenced by temperature which led to determine precisely the conditions of formation of single crystal ThO_2 microspheres. As an example, they were prepared after 20 min. of heat treatment at 1275°C or 15 min. at 1300°C. Nevertheless, it is important to note that these results were obtained for particles with a diameter close to 300 nm and that the microspheres size could also affect the kinetics of crystallite growth. In these conditions, the smaller the initial microspheres, the faster the formation of single crystal particles.

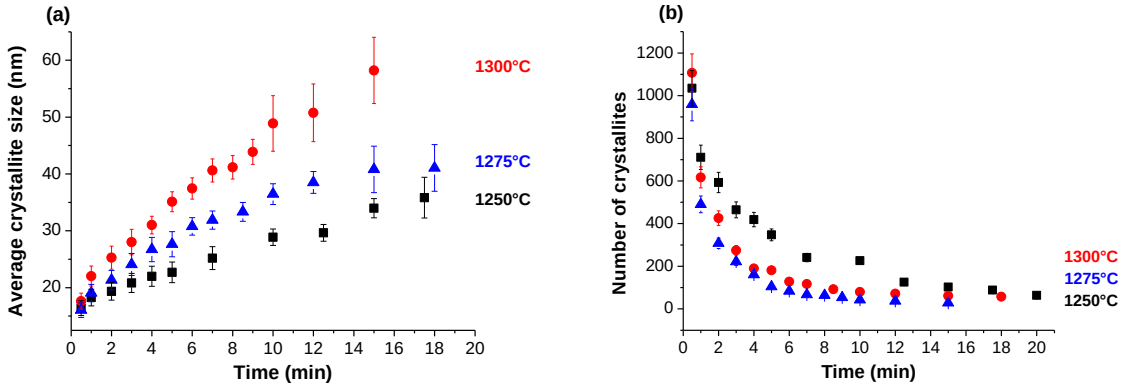

Figure 4 : Evolution of : (a) the average crystallite size and (b) the crystallite number in isolated ThO_2 microspheres during heat treatment at different temperatures.

Different mathematical functions were further tested to fit the evolution of the crystallite number within an isolated ThO_2 microsphere. Johnson-Mehl-Avrami model was first considered, due to its wide use in the field of recrystallization processes [52]. However, the need for an accurate value of the initial number of crystallites was precluded by the lack of resolution of HT-ESEM images in the early times of the heat treatment (mainly due to the very rapid evolution of the system). In a similar way, and as already stated in our previous works [44], a simple exponential law did not account for the crystallite size evolution for the longest heating times. A combination of two exponentials was then used for the fitting procedure :

$$N = N_0 - A_1.\exp(-k_1 t) - A_2.\exp(-k_2 t) \qquad (1.)$$

With N the crystallites number, N_0 the initial crystallites number, k_1 and k_2 the kinetic constants corresponding to the prevailing mechanism for short and long-term heat treatments, respectively, and A_1 and A_2 the corresponding pre-exponential factors.
Such a mathematical treatment is thus well suited to cope with the existence of two distinct and consecutive mechanisms for crystallite growth. Afterwards, the data were then systematically split into two sets corresponding to short and long-term heat durations. The corresponding kinetic data are gathered in **Table 1** and were further reported in Arrhenius diagrams to determine associated activation energies (**Figure 5**).

Table 1 : Kinetic constants obtained from the variation of the crystallites number within isolated ThO_2 microspheres using a double exponential model ($N = N_0 - A_1.\exp(-k_1t) - A_2.\exp(-k_2t)$).

Temperature (°C)	Short term		Long term	
	k_1	ln (k_1)	k_2	ln (k_2)
1200	0.09	-2.39	0.35	-1.01
1225	0.12	-2.11	0.71	-0.33
1250	0.15	-1.85	1.66	0.51
1275	0.20	-1.60	2.00	0.69
1300	0.26	-1.33	3.33	1.20

For short-term heat treatments, the activation energy linked with the crystallite growth was found to be equal to 205 ± 10 kJ.mol^{-1} and cannot be clearly ascribed to a precise growth mechanism. Indeed, two cases can be envisaged. On the one hand, a mechanical rearrangement of the crystallites can occur, provided residual porosity is still present in the aggregate. The rotation of the particles then led to the alignment of crystalline networks. Such a process, usually depicted in the literature as Oriented Attachment (OA), is generally associated to low values of activation energies, typically ranging between 50 and 100 kJ.mol^{-1} [44,53,54]. Its contribution was also already evidenced during the growth of ThO_2 nanosized crystallites of about 5 nm [15]. On the other hand, crystallites can also grow through common Otswald ripening, driven by solid-state diffusion. Even if very few studies dealt with this process in the case of elementary crystallites, one can rely on the activation energies reported in the case of grain growth during solid-state sintering, which generally range from 400 to 600 kJ.mol^{-1} for actinide dioxides [55]. On this basis, the crystallite growth within ThO_2 samples probably proceeds through both OA and diffusion mechanisms during short-term heat treatments. This combination of processes could be linked to the residual porosity of the microspheres after dehydration of the initial $ThO_2.2H_2O$ precursor.

Conversely, for long-term heat treatments, the elimination of the residual porosity precluded the rotation of the crystallites, then the contribution of the oriented attachment mechanism. This modification was associated to a significant increase in the activation energy, which rose up to 420 ± 25 kJ.mol^{-1}. This value was found to be in good agreement with that recently obtained by Clavier *et al.* during the study of bulk ThO_2 sintering (435 ± 25 kJ.mol^{-1}) [22], thus evidencing that crystallites growth became essentially driven by solid-state diffusion. Such a process led to the progressive elimination of the smallest crystallites to the benefit of

the biggest ones, the crystallite growth within the microspheres being in this case similar to that of grains within a powder agglomerate.

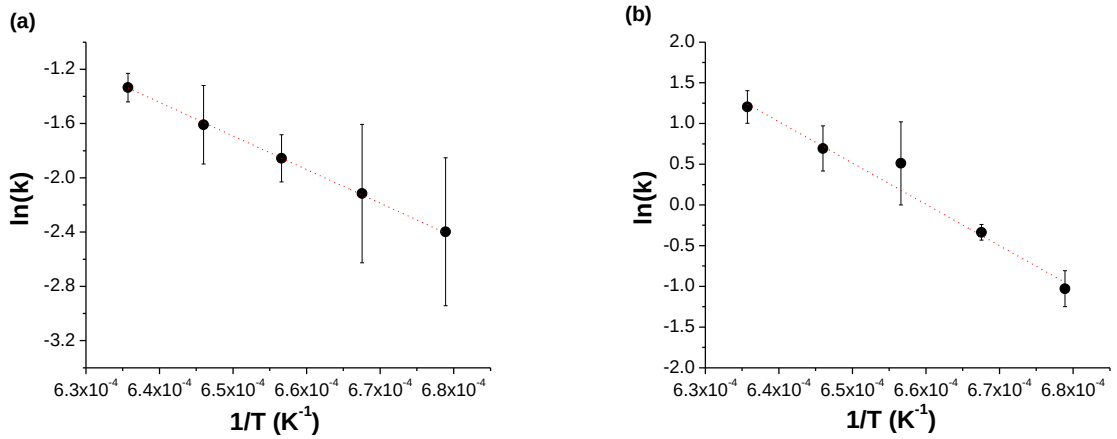

Figure 5 : Arrhenius diagrams associated to the crystallite growth within isolated ThO_2 microspheres in the 1200-1300°C range : (a) short-term and (b) long-term heat treatments.

3.2. Sintering of two-grain systems

3.2.1. Microstructural evolution

The study of the first stage of sintering for ThO_2 microspheres was performed by using both *in situ* and *ex situ* ESEM methods. In each case, the morphological modifications occurring on a pair of microspheres were observed during isothermal heat treatments performed between 1175 °C and 1300 °C. Moreover, two different kinds of particles were investigated. Indeed, the systems built from two polycrystalline grains (obtained after holding raw powder 30 min. at 850-900°C in the microscope furnace) were compared to assemblies of two single crystal microspheres, prepared after heat treatment of polycrystalline grains at 1300°C during 30 min.

The ESEM images presented on **Figure 6** show the evolution of single crystal and polycrystalline systems during heat treatment at 1275°C. The formation and growth of a neck between the microspheres was observed in both cases. Nevertheless, for all sintering temperatures studied, the neck growth was systematically more pronounced in the case of polycrystalline particles. For example, the neck between polycrystalline grains reached about 150 nm after 7 min. of heat treatment at 1275 °C whereas it was only 105 nm for single crystal grains in the same operating conditions.

For polycrystalline particles, the neck growth was simultaneously accompanied by the gradual decrease in the number of crystallites within each microsphere, as previously observed during heat treatment of isolated ThO_2 microspheres. Indeed, after 1 min of heat treatment at 1275°C, the mean size of crystallites inside each microsphere was about 20 nm and reached up to 90 nm after 5 min. The evolution of the average crystallite size was then compared to the data previously determined for isolated microspheres **(Figure 7)**. Both data sets appeared in very good agreement, thus showing that the formation and growth of a neck between the grains did not influence the general evolution of crystallites size during heating. Both

phenomena then cannot be considered to be in competition, but more likely as complementary mechanisms promoting the evolution of the system towards a reduction of its total Gibbs energy.

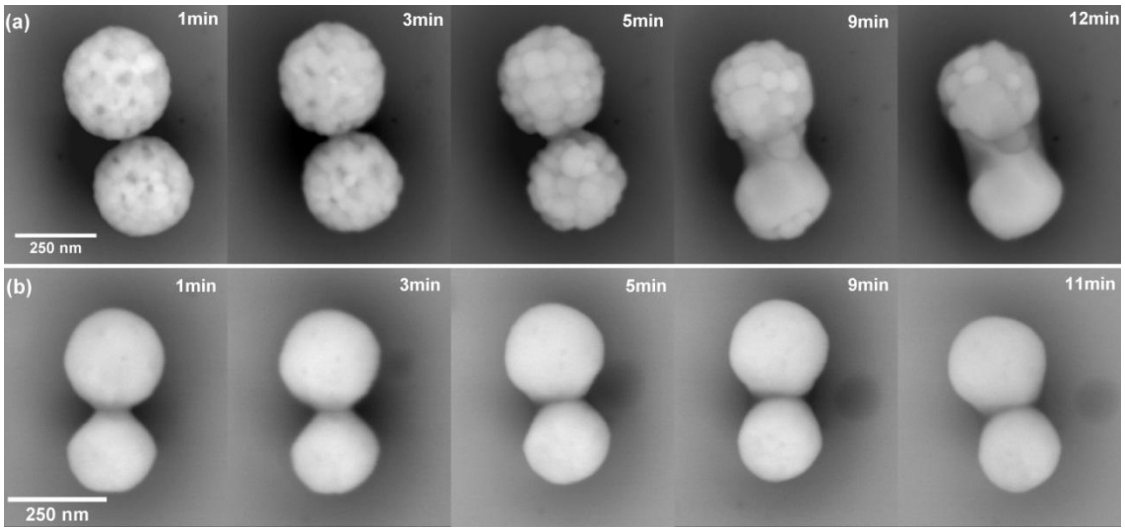

Figure 6 : ESEM micrographs of morphological modifications of ThO_2 microspheres during sintering at 1275°C: (a) polycrystalline material and (b) single-crystal particles.

However, it is important to note that for long-term heat treatments of polycrystalline systems, neck formation and crystallites growth within the microspheres led to the formation of large grains between the initial particles. Indeed, as it can be seen in **Figure 6a**, the neck between the polycrystalline microspheres (or grain boundary) is no longer clearly identifiable after 9 min. of heating at 1275 °C. This behavior then strongly differs from that observed during previous experimental studies [31,56], and was to our knowledge never described through numerical simulations [25,26,27]. On this basis, the quantitative data extracted from the ESEM micrographs were systematically split into two sets for polycrystalline systems, corresponding to the regular development of necks between the microspheres, on the one hand, and to the apparition of intermediate large crystallites, on the other hand.

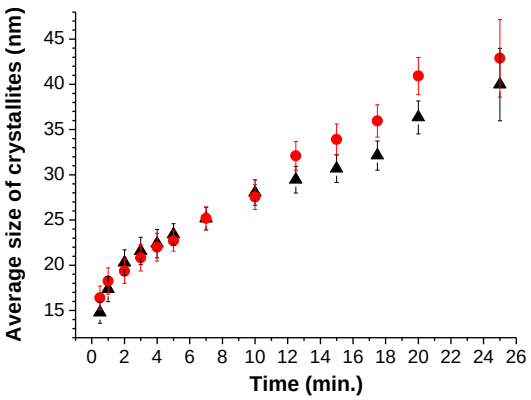

Figure 7 : Evolution of mean size of crystallites during heating of ThO_2 microspheres at T=1250°C for a single grain system (▲) and for a system constituted by two grains in contact (●).

3.2.2. Evolution of parameters of interest

The ESEM images recorded during the sintering of ThO_2 microspheres at different temperatures were then processed to determine the evolution of several parameters generally used for the description of the first step of sintering. As previously detailed, both Fiji and custom ImageJu software were used in order to evaluate for each micrograph recorded the values of the neck size, grain radius, dihedral angles and distance between grains centers (**Figure 2b)**. An example of the results obtained for a heat treatment performed at 1250°C is presented in **Figure 8**.

The evolution of neck radius is reported in **Figure 8a** for both systems studied and respectively constituted by two polycrystalline ($r \approx 160$ nm) and two single crystal grains ($r \approx 130$ nm). For the single crystals, the neck grew fast during the first 12 min. of heat treatment then reached a steady-state for a value close to 60 nm. For polycrystalline particles, the neck was found to grow faster within the 10 first minutes of heat treatment for which a clear grain boundary can be defined. For longer heating times, which correspond to the formation of intermediate crystallites between the initial microspheres, the neck size was geometrically defined as the radius of the grain assembly at the mid-distance between grain centers. This value was then found to keep increasing, and no equilibrium state was reached. Once again, only the single crystal grains presented a topological evolution comparable to that generally described by modelling [26]. Conversely, polycrystalline particles presented a quasi-linear trend in the neck size evolution which cannot be fitted using the mathematical models available in the literature.

Significant differences between single crystal and polycrystalline grain assemblies were also evidenced when plotting the evolution of the distance between grain centers (**Figure 8b**). In both cases, the decrease of this distance led to the densification of the two-grain systems [57,58]. Such a tendency was previously observed during both experimental and theoretical studies of the first stage of sintering [26,59,60] and can be assimilated to the shrinkage of compacts during sintering. Nevertheless, if a comparable relative shrinkage of about 3% was measured for the two systems studied in the first minutes of the heat treatment, it was found to diverge with the formation of intermediate grains within polycrystalline particles. In this case, the elimination of a clear grain boundary between the microspheres was then correlated to an acceleration of the densification. As a matter of evidence, the final relative shrinkage measured after 25 min. of heating at 1250°C reached about 12% for polycrystalline systems while it was only 6% for single crystals. Such a difference may be due to the elimination of porosity and to the progressive rearrangement of matter (because of crystallite growth) within polycrystalline grains systems. Moreover, it is to be noticed that such phenomenon was also observed by Lange during the sintering of compacts constituted either by polycrystalline or single crystal grains [59].

Conversely, the evolution of the other parameters studied was found to be almost independent of the initial microstructure of the spherical ThO_2 particles. Notably, the variation of the grains radii is quite similar for both systems studied, the decrease of the relative grains radii (r/r_0) reaching about 4% after 15 min. of heat treatment at 1250°C (**Figure 8c**). Such decrease in the grains size can be ascribed to the intergranular rearrangement driven by the pore and

defect elimination inside the microspheres during heating, especially in the case of polycrystalline grains [31,44]. Nevertheless, it appeared to be very limited, and owing to the uncertainties associated to the measure, the grains radii were considered as constant during the heat treatments.

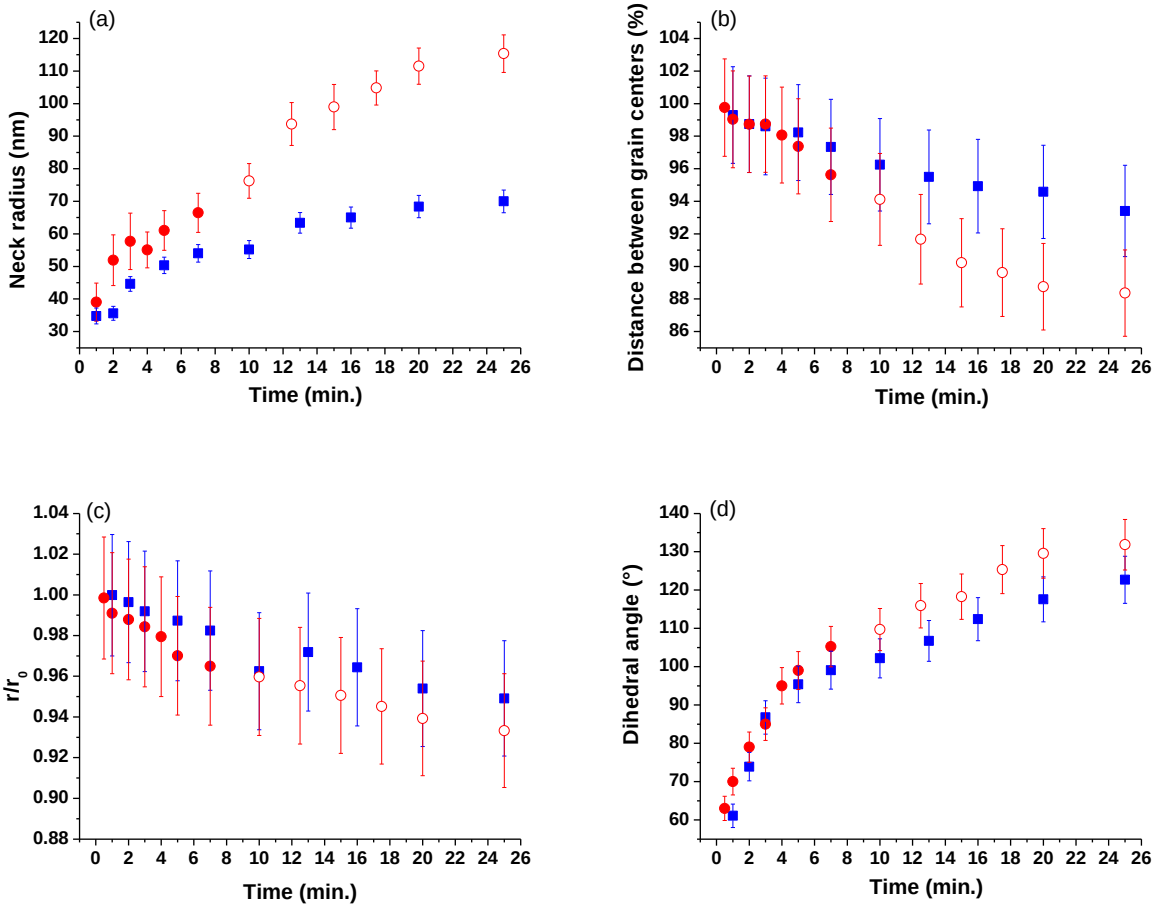

Figure 8 : Evolution of different parameters of interest during sintering of polycrystalline (●/○) and single crystal (■) ThO_2 microspheres at 1250°C: (a) neck radius, (b) distance between grain centers, (c) grain radii and (b) dihedral angles. Open symbols mark the absence of clear grain boundary in polycrystalline systems.

Likewise, the increase in the angle formed by the two grains contact in the neck region (**Figure 8d)** was similar for both systems investigated. For a single crystal assembly, which correspond to that used in numerical models for the description of the first stage of sintering, this angle is generally referred to as the dihedral angle and its value is driven by the equilibrium of forces at the triple point between two crystals in contact and air. Hence, this value does not reflect a strict physical reality for polycrystalline grains systems since there is many dihedral angles in the neck region, characterized by several crystal/crystal/air triple junctions. For the polycrystalline grains, the angle determined during this study was then the angle formed by the two microspheres contact in neck region.

3.2.3. *Neck growth mechanisms and associated activation energies*

The evolution of neck's size during the first stage of sintering is generally represented by a dimensionless parameter (λ), which makes it possible to compare the sintering degree between systems constituted by grains of different sizes. This parameter is defined as the ratio of neck size (x) and average grains radii ($r = (r_1+r_2)/2$): $\lambda = x/r$ [61,62]. Its evolution determined from image processing was plotted for the systems and sintering temperatures investigated. The data obtained at 1250°C are represented in **Figure 9** as an example for the general trend of the evolution of this parameter during heat treatment.

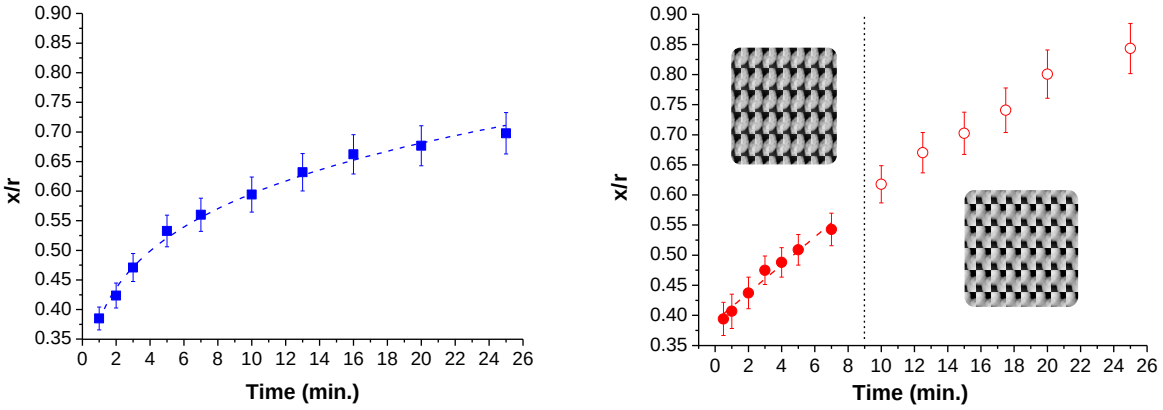

Figure 9 : Evolution of the sintering degree (λ = x/r) during sintering of two ThO_2 single crystal (■) and polycrystalline (●) microspheres at T = 1250°C. Fitting of the data was performed using a linear law for the polycrystalline grains and the general kinetic law of neck growth for single crystal grains. Open symbols marks the absence of clear grain boundary in polycrystalline systems.

As already observed for neck size, and in good agreement with the results previously reported for CeO_2 [31], the sintering degree appeared systematically higher for the polycrystalline grains than for the single crystal grains whatever the heating temperature. The evolution of λ then appears to be mostly driven by the variation of neck size, since the decrease of grains radii could be neglected for both systems. In these conditions, similar variations as those detailed for x value were observed here. For polycrystalline grains, the evolution of the sintering degree during short-term heat treatment could be considered as linear, until a value close to 0.6 was reached. Interestingly, such value of the sintering degree is generally reported to mark the transition from the first to the second stage of the sintering process, *i.e.* from neck formation to porosity elimination [61]. The end of the first stage of sintering could then be correlated with the apparition of large crystallites between the initial microspheres, in place of the well-defined grain boundary. In this configuration, the elementary particles composing the microspheres kept growing, making the crystallites present in the neck region unable to maintain an equilibrium configuration [31,56]. Conversely, single crystal grains presented an evolution in good agreement with that usually reported for the description of the first stage of sintering [57,63]. In this case, reaching a sintering degree close to $\lambda = 0.6$ barely corresponded to establishment of a steady-state. The initial microstructure of the powders (*i.e.* level of

polycrystallinity) then turns out to be an important parameter to be taken into account during both experimental and numerical studies, that can influence the sintering behavior both at the microscopic and macroscopic scales [49].

In order to determine the kinetics data representative of the phenomena occurring during the first stage of sintering, the curves obtained after image processing for each isothermal treatment performed between 1175°C and 1300°C were fitted using different analytical laws. For single crystal grains, an analytical model describing the theoretical evolution of the sample during the first stage of sintering is available in the literature. Such a general model is usually employed at the macroscopic scale [61] to describe the linear shrinkage of a pellet during sintering. During the last few years, this law was mostly used in the field of ceramic materials, for the identification of diffusion mechanisms occurring during sintering of bulk samples, for example by using the master sintering curve approach [64,65] or Dorn's method [66]. The general law of neck growth was used for the first time at the microscopic level, for ceramic materials, during the sintering of cerium dioxide and has led to the determination of kinetics data and the identification of mechanisms of the neck elaboration [31]. This general law of neck growth, reported as equation 2 [67,68,69], was thus used for determination of kinetics constants at all the temperatures studied :

$$\lambda^{n} = \frac{k.t}{r^{m}} \qquad (2.)$$

where $\lambda = x/r$ denotes the sintering degree, k is the kinetic constant, t is the duration of heat treatment, and n and m are exponents characteristic of the diffusion process involved (i.e. mainly surface, volume or grain boundary diffusion).

Moreover, as the grain radii variation during the various heat treatments performed was found to be negligible, the r^m term could be supposed to remain almost unchanged, which led to the definition of an apparent kinetic constant k' such as :

$$\lambda = \left(\frac{k.t}{r^{m}}\right)^{1/n} = (k'.t)^{1/n} \qquad (3.)$$

The kinetic constants (k and k') determined for the systems composed by two single-crystals in contact (reported in **Table 2**) were then plotted into an Arrhenius diagram in order to determine the activation energy corresponding to the mechanisms associated to the first stage of ThO_2 sintering (**Figure 10a**) and led to a value of 620 ± 40 kJ.mol^{-1}. This value is clearly located in the upper range of activation energies reported by various authors for the sintering of bulk thorium oxide, which typically varies from 435 ± 25 kJ.mol^{-1} [22] to 650 kJ.mol^{-1} [70,71]. As such variability cannot be ascribed to redox reactions, Th(IV) being the only stable oxidation state for this element, it could then be suggested that the polycrystallinity of the powders could impact the activation energy of the sintering. Indeed, literature already emphasized the role of dislocations as diffusion short circuits in ThO_2 single crystals [72]. The highest value of activation could then be correlated to single crystal particles for which only solid-state diffusion is available to promote the establishment of neck between the grains, then the grain growth.

Table 2 : Values of kinetic constants obtained during sintering of polycrystalline grains with a linear law ($\lambda = k.t + \lambda_0$) and single crystal grains with the law of neck growth ($\lambda^n = \frac{k.t}{r^m}$). The values of the n exponent are also provided for single crystal systems.

Temperature (°C)	Single crystal grains				Polycrystalline grains	
	$k' = (k/r^m)^{1/n}$	k	ln(k)	n	k	ln(k)
1175	0.25	1.32×10^6	14.09	5.5 ± 0.6	-	-
1200	0.29	2.56×10^6	14.75	5.5 ± 0.5	0.002	-6.02
1225	0.35	5.41×10^6	15.50	5.0 ± 0.7	0.004	-5.37
1250	0.38	1.80×10^7	16.70	5.3 ± 0.5	0.011	-4.48
1275	0.41	3.09×10^7	17.24	5.0 ± 0.8	0.015	-4.14
1300	-	-	-	-	0.027	-3.60

The fit of the λ evolution thanks to equation 3 was also used to determine the diffusion path operating during the establishment of the neck. Indeed, five different processes are usually supposed to drive sintering, and characterized by specific n values with n = 2 for viscous flow; n = 3 for evaporation-condensation; n = 4 for volume diffusion; n = 7 for surface diffusion and n = 6 for grain boundary diffusion [73,74,75]. Among these mass transport mechanisms, only three lead to the densification of the samples (i.e. for two grains systems, the decrease of distance between the centers of the grains): viscous flow (during liquid phase sintering), grain boundary diffusion and volume diffusion. In the case of the system constituted by single crystalline grains, the values of the n exponent determined at different sintering temperatures (**Table 2**) appeared to be systematically close to 6. As a matter of fact, the sintering of two single crystal ThO_2 microspheres is then driven by a grain boundary diffusion mechanism. This prevailing mechanism is in good agreement with the morphological modification occurring on sample during heat treatment, i.e. the neck elaboration and the densification (decrease of the distance between grains centers) (**Figure 8**).

For the polycrystalline grains systems, the general law of neck growth reported above cannot be used for the description of the evolution of sintering degree. Indeed, this equation was developed based on the hypothesis of single crystal grains, which is obviously far from this system. As no model is currently available in the literature which could allow us to fit the data obtained for polycrystalline microspheres in contact, a simple linear law (see equation 4), corresponding to the trend observed for short-term heat treatments, was used for the determination of kinetic constants.

$$\lambda = k.t + \lambda_0 \qquad (4.)$$

Where $\lambda = x/r$ denotes the sintering degree, λ_0 the sintering degree at t = 0 (beginning of the isothermal plateau), k is a kinetic constant and t is the duration of heat treatment.

It is then important to underline that this law was only applied in the section of the curves corresponding to micrographs where the neck (or grain boundary) is clearly identifiable between the two microspheres (**Figure 9**). The activation energy determined in this case from the kinetics constants values (**Table 2**) was about 446 ± 38 kJ.mol^{-1} (**Figure 10b**). Conversely to the value determined for single crystals, it is clearly located in the lower limit of the wide range of the values reported in the literature by various authors for sintering of ThO_2 bulk materials [22,70,71]. The determination of a lower activation energy, compared to single crystal grains, is mainly due to the presence of several crystallites within the microspheres, which probably affects the nature of mechanisms occurring during sintering. A similar behavior was already observed during the first stage of CeO_2 sintering, for which activation energies of 186 ± 31 kJ.mol^{-1} and 516 ± 27 kJ.mol^{-1} were obtained for polycrystalline and single crystal two-grain systems, respectively [31]. This difference was assigned to the contribution of two mechanisms occurring simultaneously during sintering of polycrystalline grains, i.e. oriented attachment at the beginning of heat treatment, followed by solid-state diffusion.

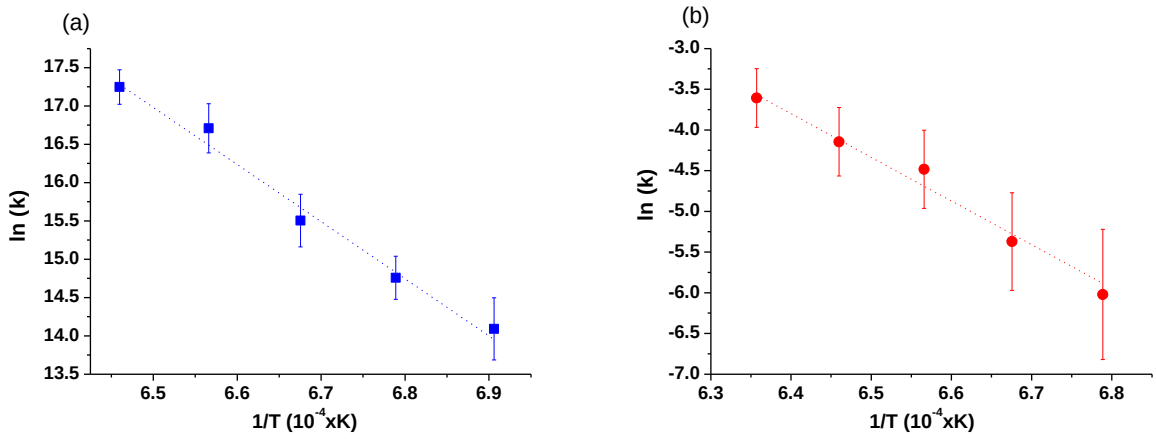

Figure 10 : Arrhenius diagram and activation energies determined during sintering at different temperatures (between 1050°C – 1225°C) for (a) single crystal grains (■) and (b) polycrystalline grains (●).

Also, it was already demonstrated that oriented attachment can lead to the initial elaboration of necks between CeO_2 particles through the reorganization of crystalline planes in the same orientation [76,77]. This process was made possible because of the nanosize of the crystallites, associated with a high degree of freedom in the region of contact between the two microspheres, which promotes the formation of a continuous lattice (neck). Furthermore, this mechanism is generally associated with low activation energies, of about one hundred of kiloJoule per mole [44,53,54]. The difference between the activation energies determined for the sintering of polycrystalline and single-crystal ThO_2 can be unambiguously assigned to the

contribution of oriented attachment at the beginning of heat treatments, when the crystallites constituting the microspheres present a nanoscale size.

However, the contribution of this mechanism is probably low, especially when compared to the data previously obtained for CeO_2 [44], as attested by the small difference between activation energies obtained for the two systems studied (less than 200 $kJ.mol^{-1}$). Since these oxides present a similar crystal structure (fluorite-type face centered cubic, Fm-3m space group) and comparable grain sizes (between 400 nm and 600 nm), this difference could be explained by the initial precursors synthesized in both cases. Indeed, an oxocarbonate precursor ($Ce_2O(CO_3)_2.nH_2O$) was precipitated for CeO_2 [78] while hydrated thorium oxide ($ThO_2.2H_2O$) was directly prepared for ThO_2. The thermal conversion of these precursors into oxides then led to drastically different weight losses, which appeared higher for cerium oxocarbonate (above 20 %) [78] than for hydrated thorium oxide (approx. 12%). The thermal conversion of these precursors to oxides then probably led to the formation of different quantities of residual porosity, which directly impacts the degree of freedom of the crystallites within the microspheres. The method used for powder preparation can then be correlated to the different contributions of oriented attachment mechanism during the sintering of CeO_2 and ThO_2 polycrystalline microspheres.

In these conditions, general guidelines for the preparation of powders with high sintering capability could be drawn from these results. Indeed, a decrease of the activation energy associated to sintering, which should lead to a decrease of the temperature required for the complete densification of a bulk sample, was observed :

- when the samples present a high level of polycrystallinity, i.e. when they are constituted by nanosized crystallites, whatever the size of the agglomerates they are constituting;
- when the samples bear significant amount of residual porosity, which allows the mechanical reorientation of crystallites (oriented attachment) to assist solid-state diffusion in the establishment of grains.

These recommendations then back up the innovative ways of preparation currently under investigation for the fabrication of nuclear fuels for the next generation of reactors. Indeed, they are frequently based on the co-precipitation of actinides (such as uranium and plutonium) as low-temperature precursors that led to the desired oxide phase after thermal conversion. In this framework, oxalate compounds were particularly investigated [79] and were shown to produce oxide powders with residual mesoporosity [37] and small crystallite size [80]. The importance of these characteristics in the mechanisms operating during densification could then explain the good sintering capability always stated for powders issued from oxalate precursors [81].

4. Conclusion

The behavior of ThO_2 microspheres during heat treatments at high temperature (typically 1100-1300°C) was investigated by electron microscopy, including HR-TEM as well as *in situ* and *ex situ* ESEM. The observation of isolated particles first allowed to describe the mechanisms driving the growth of crystallites within the microspheres. For short-term heat treatments, a combination of oriented attachment (mechanical rearrangement of the crystallites) and of solid-state diffusion was associated to an activation energy of about 200 $kJ.mol^{-1}$. For longer calcinations, solid state diffusion was the prevailing mechanisms and was correlated to a higher value of E_A, close to 400 $kJ.mol^{-1}$. In any case, the growth of crystallites led to spherical single-crystals, which conditions of preparation were determined in terms of heating time and temperature.

Both polycrystalline and single-crystal microspheres were further studied as two-grains assemblies in order to investigate the formation of necks between the particles, corresponding to the first stage of sintering. For single crystals, the topological evolution of the system was found to agree well with the models previously reported in the literature. The activation energy linked with neck growth kinetics was found to be about 600 $kJ.mol^{-1}$, indicating solid-state diffusion as the prevailing driving mechanism. Conversely, the establishment of necks between two polycrystalline microspheres was found to deviate from the expected trend. While short-term heat treatments still led to the formation of a clear grain boundary, it was further replaced by intermediate large-size crystallites for longer heating times. Such modification was mainly assigned to the initial microstructures of the particles used, which combined nanosized crystallites and a low amount of residual porosity that precludes a significant contribution of oriented attachment over the global mechanism.

The level of polycrystallinity of the powder, as well as its initial inner microstructure, which both arose from the synthesis method employed, was then found to significantly impact the kinetics linked to the first stage of sintering in a system where the influence of other parameters such as atmosphere and redox reactions can be ruled out. This study then provides new insights on the high sintering capability of the powders issued from several wet chemistry routes investigated in the framework of nuclear fuel fabrication. Similar studies have now to be undertaken in the case of samples exhibiting more complex chemical behavior, such as uranium oxides. In this case, it will be interesting to determine whether or not the parameters linked to the preparation of the powder appear of first order compared to the effects of sintering atmosphere.

Acknowledgments

Authors would like to thank X.F. Le Goff and H.P. Brau (ICSM/L2ME) for their help in the interpretation of TEM images, A. Sonzogni (ICSM/LIME) for performing BET/BJH measurements and J. Favrichon (CEA/DEN/UG-UST/STIC/GPSI) for the development of the ImageJu software. They are also grateful to the Materials Federative Project included in the NEEDS program (Nucléaire, Energie, Environnement, Déchets, Société) of CNRS for its continuous financial support. G.I. Nkou Bouala particularly thanks the JECS Trust for

supporting her participation to the 2016 ACerS Winter Workshop (grant 201363-02) and allowing the presentation of this work at ICACC 2016 Conference.

Supplementary material

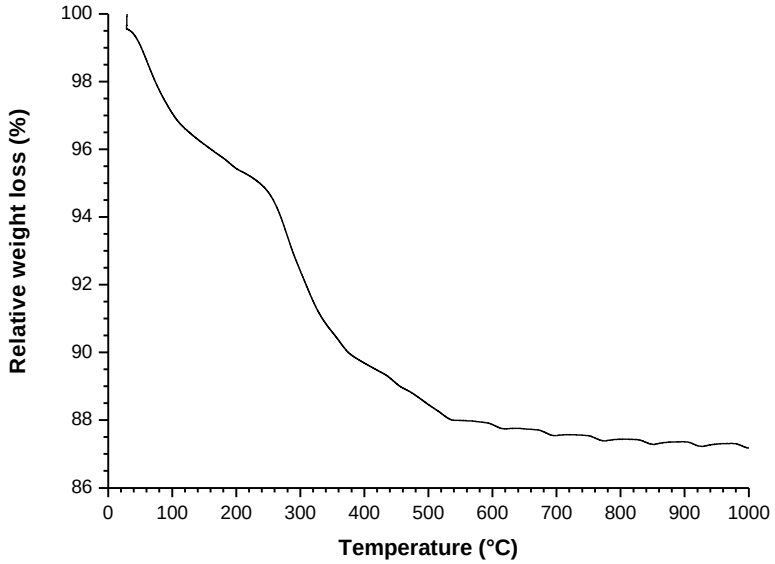

Figure S1 : TG analysis of $ThO_2.nH_2O$ precursor.

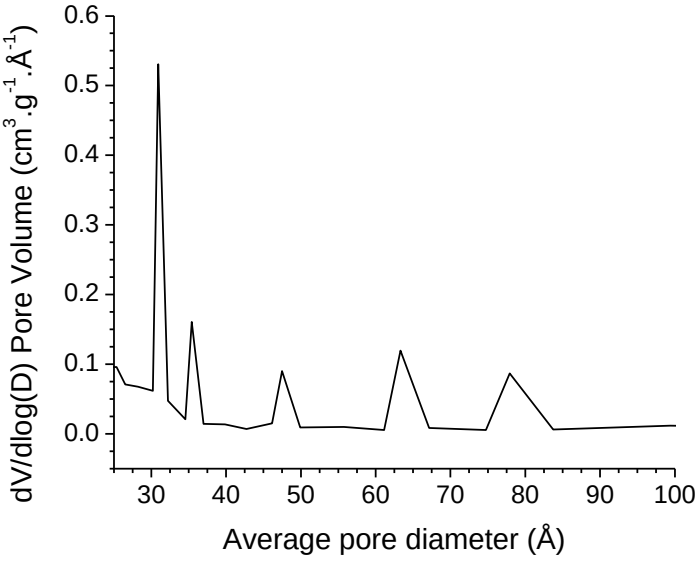

Figure S2 : Incremental pore area versus the average pore diameter for ThO_2 microspheres obtained after 4 h of heat treatment at 750°C under air.

References

1. M. Lung and O. Gremm, Perspectives of the thorium fuel cycle, *Nucl. Eng. Des.*, **180** (1998) 133-146.
2. J. Tommasi, M. Delpech, J.P. Grouiller and A. Zaetta, Long-Lived Waste Transmutation in Reactors, *Nucl. Technol.*, **111** (1995) 133-148.
3. K.I. Bjork, A BWR fuel assembly design for efficient use of plutonium in thorium–plutonium fuel, *Prog. Nucl. Energ.*, **65** (2013) 56-63.
4. J. Belle and R.M. Berman, Thorium dioxide: properties and nuclear applications, US Department of Energy Report, DOE/NE-0060 (1984).
5. R.K. Sinha and A. Kakodkar, Design and development of the AHWR—the Indian thorium fuelled innovative nuclear reactor, *Nucl. Eng. Des.*, **236** (2006) 683-700.
6. K. Anantharaman, V. Shivakumar and D. Saha, Utilisation of thorium in reactors, *J. Nucl. Mater.*, **383** (2008) 119-121.
7. Hj. Matzke, V.V. Rondinella and T. Wiss, Materials research on inert matrices: a screening study, *J. Nucl. Mater.*, **274** (1999) 47-53.
8. C. Ronchi, J.P. Ottaviani, C. Degueldre and R. Calabrese, Thermophysical properties of inert matrix fuels for actinide transmutation, *J. Nucl. Mater.*, **320** (2003) 54-65.
9. H. Akie, T. Muromura, H. Takano and S. Matsuura, A new fuel material for once-through weapons plutonium burning, *Nucl. Technol.*, **107** (1994) 182-192.
10. B. Shi, H.A. Dabbagh and B.H. Davis, Catalytic dehydration of alcohols. Kinetic isotope effect for the dehydration of t-butanol, *Top. Catal.*, **18** (2002) 259-264.
11. F. Zhuge, Z. Ye, F. Wang, Y. Wang, H. Zhang and B. Ding, Nanocomposite W–4.5% ThO_2 thermionic cathode, *Mater. Lett.*, **57** (2003) 2776-2779.
12. J.E. Kelly, Generation IV International Forum: A decade of progress through international cooperation, *Progr. Nucl. Energ.* **77** (2014) 240-246.
13. E. Schouler, A. Hammou and M. Kleitz, Complex impedance of electrochemical cells based on yttria doped thoria, *Mater. Res. Bull.*, **11** (1976) 1137-1146.
14. M. Gabard, Y. Cherkaski, N. Clavier, L. Brissonneau, M.C. Steil, J. Fouletier, A. Mesbah and N. Dacheux, Preparation, characterization and sintering of yttrium-doped ThO2 for oxygen sensors applications, *J. All. Compd.* **689** (2016) 374-382.
15. D. Hudry, C. Apostolidis, O. Walter, T. Gouder, E. Courtois, C. Kubel and D. Meyer, Controlled synthesis of thorium and uranium oxide nanocrystals, *Chem. A Europ. J.*, 19 (2013) 5297-5305.
16. M. Moeini, A. Malekazdeh, S.J. Ahmadi and M. Hosseinpour, Synthesis of thoria nanoparticles via the hydrothermal method in supercritical condition, *Mater. Lett.*, **81** (2012) 99-101.
17. T. Yousefi, M. Torab-Mostaedi, H. Sohbtzadeh, A. Reza Keshtar, H. Aghayan and M. Ghannadi Maragheh, Synthesis and characterization of ultra-fine well-dispersed thoria nano spheres through reduction reactions in nitrate bath, *Prog. Nucl. Energ.*, **85** (2015) 600-604.
18. L. Wang, R. Zhao, X. W. Wang, L. Mei, L. Y. Yuan, S. A. Wang, Z. F. Chaia and W. Q. Shi, Size-tunable synthesis of monodisperse thorium dioxide nanoparticles and their performance on the adsorption of dye molecules, *CrystEngComm*, **16** (2014) 10469–10475.
19. R. Zhao, L. Wang, Z.F. Chai, W.Q. Shi, Synthesis of ThO_2 nanostructures through a hydrothermal approach: influence of hexamethylenetetramine (HMTA) and sodium dodecyl sulfate (SDS), *RSC Adv.*, **4** (2014) 52209-52214.
20. R.D. Purohit, S. Saha and A.K. Tyagi, Nanocrystalline thoria powders via glycine-nitrate combustion, *J. Nucl. Mater.*, **288** (2001) 7-10.
21. N. Hingant, N. Clavier, N. Dacheux, S. Hubert, N. Barre, R. Podor and L. Aranda, Preparation of morphology controlled $Th_{1-x}U_xO_2$ sintered pellets from low-temperature precursors, *Powder. Technol.*, **208** (2011) 454-460.
22. N. Clavier, R. Podor, L. Deliere, J. Ravaux and N. Dacheux, Combining *in situ* HT-ESEM observations and dilatometry: An original and fast way to the sintering map of ThO_2, *J. Mater. Chem. Phys.*, **137** (2013) 742-749.
23. J. Banerjee, A. Ray, A. Kumar and S. Banerjee, Studies on sintering kinetics of ThO_2–UO pellets using master sintering curve approach, *J. Nucl. Mater.*, **443** (2013) 467-478.

24. V. Tyrpekl, M. Cologna, D. Robba and J. Somers, Sintering behaviour of nanocrystalline ThO_2 powder using spark plasma sintering, *J. Europ. Ceram. Soc.*, **36** (2016) 767-777.

25. F. Wakai and K.A. Brakke, Mechanics of sintering for coupled grain boundary and surface diffusion, *Acta. Mater.*, **59** (2001) 5379-5387.

26. J. S. Raut, R. B. Bhagat and K. A. Fichthorn, Sintering of aluminum nanoparticles: a molecular dynamics study, *Nanostruct. Mater.*, **10** (1998) 837–851.

27. W. Zhang and J.H. Schneibel, The sintering of two particles by surface and grain boundary diffusion—a two-dimensional numerical study, *Acta Metall. Mater.*, **43** (1995) 4377-4386.

28. F. Wakai, Modeling and simulation of elementary processes in ideal sintering, *J. Am. Ceram. Soc.*, **89** (2006) 1471-1484.

29. J.S. Bordère, and D. Bernard, Full resolution of the Monte Carlo time scale demonstrated through the modelling of two-amorphous-particles sintering, *Comput. Mater. Sci.*, **43** (2008) 1074-1080.

30. S. Martin, R. Parekh, M. Guessasma, J. Lechelle, J. Fortin and K. Saleh, Study of the sintering kinetics of bimodal powders : a parametric DEM study, *Powder Technol.*, **270** (2015) 637-645.

31. G.I. Nkou Bouala, N. Clavier, S. Martin, J. Léchelle, J. Favrichon, H. P. Brau, N. Dacheux, and R. Podor, From *in Situ* HT-ESEM Observations to Simulation: How Does Polycrystallinity Affects the Sintering of CeO_2 Microspheres?, *J. Phys. Chem. C*, **120** (2016) 386–395.

32. G.I. Nkou Bouala, N. Clavier, R. Podor, J. Cambedouzou, A. Mesbah, H.P. Brau, J. Léchelle and N. Dacheux, Preparation and characterisation of uranium oxides with spherical shapes and hierarchical structures, *CrystEngComm*, **16** (2014) 6944-6954.

33. S. Hubert, J. Purans, G. Heisbourg, P. Moisy and N. Dacheux, Local Structure of Actinide Dioxide Solid Solutions $Th_{1-x}U_xO_2$ and $Th_{1-x}Pu_xO_2$, *Inorg. Chem.*, 45 (2006) 3887-3894.

34. J. Martinez, N. Clavier, A. Mesbah, F. Audubert, X.F. Le Goff, N. Vigier and N. Dacheux, An original precipitation route toward the preparation and the sintering of highly reactive uranium cerium dioxide powders, *J. Nucl. Mater.*, **462** (2015) 173-181.

35. J.C. Renshaw, F.R. Livens, D. Collison, G.D. Robson, A.P.J. Trinci and R.J. Taylor, Solubilization of α-FeO(OH), $ThO_2.2H_2O$ and γ-UO_3 by hydroxamate and carboxylate Hgands, *J. Nucl. Sci. Technol.*, **39** (2002) 251-254.

36. E.P. Barret, L.G. Joyner and P.H. Halenda, The determination of pore volume and area distributions in porous substances. I. Computations from nitrogen isotherms, *J. Am. Chem. Soc.*, **73** (1951) 373-380.

37. L. Claparede, N. Clavier, N. Dacheux, P. Moisy, R. Podor, J. Ravaux, Influence of crystallization state and microstructure on the chemical durability of Cerium–Neodymium mixed oxides, *Inorg. Chem.*, **50** (2011) 9059-9072.

38. L. Joly-Pottuz, A. Bogner, A. Lasalle, A. Malchere, G. Thollet, S. Deville, Improvements for imaging ceramics sintering in situ in ESEM, *J. Microsc.*, **244** (2011) 93–100.

39. R. W. Knowles and T. A. Hardt, High temperature specimen stage and detector for an environmental scanning electron microscope, *US Patents*, 525–592 (1996).

40. R. Podor, D. Pailhon, J. Ravaux and H.P. Brau, Development of an integrated thermocouple for the accurate sample temperature measurement during high temperature environmental scanning electron microscopy (HT-ESEM) experiments, *Microsc. Microanal.*, **21** (2015) 307-312.

41. A. Baena, T. Cardinaels, J. Vleugels, K. Binnemans and M. Verwerft, Activated sintering of ThO_2 with Al_2O_3 under reducing and oxidizing conditions, *J. Nucl. Mater.*, **470** (2016) 34-43.

42. R. Podor, H. P. Brau and J. Ravaux, In situ experiments in the scanning electron microscope chamber, in : *Scanning Electron Microscopy*, V. Kazmiruk (Ed.), *InTech*, 2012.

43. S. Ebnesajjad, Handbook of Adhesives and Surface Preparation, *Elsevier*, *Amsterdam*, 2011.

44. G. I. Nkou Bouala, N. Clavier, J. Léchelle, A. Mesbah, N. Dacheux, R. Podor, *In situ* HT-ESEM study of crystallites growth within CeO_2 microspheres, *Ceram. Intern.*, **41** (2015) 14703.

45. ImageJ: Wayne Rasband, http://rsbweb.nih.gov/ij/ (accessed 23.07.2016).

46. M.D. Abramoff, P.J. Magalhães and R. J. Sunanda, Image processing with ImageJ, *Biophotonics Intern.*, **11** (2004) 36–42.

47. J. Pascau and J.M. Mateos Pérez, Image Processing with ImageJ, *Packt publishing Ltd*, *Birmingham*, 2013.

48. J. Favrichon / Imageju, https://github.com/jfavrichon/imageju (accessed 23.07.2016).

49. E. A. Anumol, B. Viswanath, P. G. Ganesan, Y. Shi, G. Ramanath and N. Ravishankar, Surface diffusion driven nanoshell formation by controlled sintering of mesoporous nanoparticle aggregates, *Nanoscale*, **2** (2010) 1423–1425.

50. A.K. Srivastava, P. Tiwari and R.V. Nandedkar, TEM studies on the formation of nano crystallites of Si by metal induced crystallization, *Solid State Comm.*, **137** (2006) 400–404.

51. S. J. Yoo, C. Y. Kim, J. W. Shin, S. G. Lee, J. M. Jeong, Y. J. Kim, S. H. Lee and J. G. Kim, Characterization of an amorphous carbon film covering a Mo grid during in situ heating TEM study, *Mater. Charac.*, **78** (2013) 31–36.

52. C. Tamain, F. Garrido, L. Thome, N. Dacheux and A. Ozgumus, Structural behavior of β-thorium phosphate diphosphate (β-TPD) irradiated with ion beams, *J. Nucl. Mater.*, **373** (2008) 378-386.

53. P. Scardi, M. Leoni, M. Mueller and R. Di Maggio, In situ size-strain analysis of nanocrystalline ceria growth, *Mater. Science Eng. A*, **528** (2010) 77–82.

54. H. Zhang and J. F. Banfield, Kinetics of crystallization and crystal growth of nanocrystalline anatase in nanometer-sized amorphous titania, *J. Chem. mater.*, **14** (2002) 4145–4154 (2002).

55. N. Clavier, G.I. Nkou Bouala, J. Léchelle, J. Martinez, N. Dacheux, R. Podor, Novel approaches for the in situ study of the sintering of nuclear oxide fuel materials and their surrogates, *Radiochim. Acta*, submitted (2016).

56. E. B. Slamovich and F. F. Lange, Densification Behavior of Single-Crystal and Polycrystalline Spherical Particles of Zirconia, *J. Am. Ceram. Soc.*, **73** (1990) 3368-3375.

57. G. C Kuczynski, The mechanism of densification during sintering of metallic particles, *Acta Metall.*, **4** (1956) 58–61.

58. F. B. Swinkels and M. F. Ashby, A second report on sintering diagrams, *Acta Metall.*, **29** (1981) 259–281.

59. F. F. Lange, Densification of powder compacts: An unfinished story, *J. Eur. Ceram. Soc.*, **28** (2008) 1509–1516.

60. W. Zhang and J. H. Schneibel, The sintering of two particles by surface and grain boundary diffusion—a two-dimensional numerical study, *Acta Metall. Mater.*, **43** (1995) 4377–4386.

61. S.J. L. Kang, Sintering: Densification Grain Growth and Microstructure, *Elsevier Butterworth-Heinemann, Oxford*, 2005.

62. W. K. Lee, R. L. Eadie, G. C. Weatherly and K. T. Aust, A study of the sintering of spherical silver powder—II. The initial stage, *Acta Metall.*, **26** (1978) 1837-1843.

63. M. A. Asoro, P. J. Ferreira and D. Kovar, In situ transmission electron microscopy and scanning transmission electron microscopy studies of sintering of Ag and Pt nanoparticles, *Acta Mater.*, **81** (2014) 173–183.

64. T. R. G. Kutty, K. B. Khan, P. V. Hegde, J. Banerjee, A. K. Sengupta, S. Majumdar and H. S. Kamath, Development of a master sintering curve for ThO_2, *J. Nuclear Mater.*, 327 (2004) 211–219.

65. H. Su and D L Johnson, Sintering of alumina in microwave-induced oxygen plasma, *J. Am. Ceram. Soc.*, **79** (1996) 3199–3210.

66. P. Dehaudt, L. Bourgeois and H. Chevrel, Activation energy of UO_2 and UO_{2+x} sintering, *J. Nucl. Mater.*, **299** (2001) 250-259.

67. R. M. German, Sintering: from Empirical Observations to Scientific Principles, *Elsevier Butterworth-Heinemann, Oxford*, 2014.

68. D. Bernache-Assolant, Chimie-physique du frittage, *Hermes, Paris*, 1993.

69. D. Kuroiwa, A study of ice sintering, *Tellus*, **13** (1961) 252–259.

70. Hj. Matzke, On uranium self-diffusion in UO_2 and UO_{2+x}, *J. Nucl. Mater.*, **30** (1969) 26-35.

71. K. Shiba, Diffusion Processes in Nuclear Materials, *North Holland, Amsterdam*, 1992.

72. A.D. King, Thorium diffusion in thoria and urania, Atomic Energy of Canada Limited report, AECL-3655, 1970.

73. C.A. Handwerker, Sintering and grain growth of MgO, *PhD thesis, Massachusetts Institute of Technology*, 1983.

74. G. H. Gessinger, Volume diffusion as densification rate-controlling step in sintering, *Scripta Metall.*, **4** (1970) 673-675.

75. M. F. Ashby, A first report on sintering diagrams, *Acta Metall.*, **22** (1974) 275-289.

76. J. Zhang, F. Huang and Z. Lin, Progress of nanocrystalline growth kinetics based on oriented attachment, *Nanoscale*, **2** (2009) 18–34.

77. R. L. Penn and J. F. Banfield, Imperfect oriented attachment: dislocation generation in defect-free nanocrystals, *Science*, **281** (1998) 969–971.

78. S. Wang, F. Gu, C. Li and H. Gao, Shape-controlled synthesis of $CeOHCO_3$ and CeO_2 microstructures, *J. Cryst. Growth*, **307** (2007) 386–394.

79. F. Abraham, B. Arab-Chapelet, M. Rivenet, C. Tamain, S. Grandjean, Actinide oxalates, solid state structures and applications, *Coord. Chem. Rev.*, **266-267** (2014) 28-68.

80. L. Claparede, N. Clavier, N. Dacheux, A. Mesbah, J. Martinez, S. Szenknect, P. Moisy, Multiparametric dissolution of thorium–cerium dioxide solid solutions, *Inorg. Chem.*, **50** (2011) 11702-11714.

81. G.D. White, L.A. Bray and P.E. Hart, Optimization of thorium oxalate precipitation conditions relative to derived oxide sinterability, *J. Nucl. Mater.*, **96** (1981) 305-313.